JGR Oceans

RESEARCH ARTICLE
10.1029/2019JC015470

Key Points:
- SST-SSH correlations over eddies are not always positive
- Composite heat flux pattern over eddies is asymmetric and similar to SST
- Coupling strength between SST and heat flux is 46.8 (48.0) W/m^2 per degree over AEs (CEs)

Correspondence to:
L. Yu,
lyu@whoi.edu

Citation:
Liu, Y., Yu, L., & Chen, G. (2020). Characterization of sea surface temperature and air-sea heat flux anomalies associated with mesoscale eddies in the South China Sea. *Journal of Geophysical Research: Oceans*, *125*, e2019JC015470. https://doi.org/10.1029/2019JC015470

Received 12 JUL 2019
Accepted 11 MAR 2020
Accepted article online 16 MAR 2020

Characterization of Sea Surface Temperature and Air-Sea Heat Flux Anomalies Associated With Mesoscale Eddies in the South China Sea

Yingjie Liu[1,2], Lisan Yu[3], and Ge Chen[1]

[1]College of Information Science and Engineering, Ocean University of China, Qingdao, China, [2]CAS Key Laboratory of Ocean Circulation and Waves, Institute of Oceanology, Chinese Academy of Sciences and Center for Ocean Mega-Science, Chinese Academy of Sciences, Qingdao, China, [3]Department of Physical Oceanography, Woods Hole Oceanographic Institution, Woods Hole, MA, USA

Abstract This study is to quantify the effects of mesoscale eddies on air-sea heat fluxes and related air-sea variables in the South China Sea. Using satellite observations of sea surface temperature (SST) and sea surface height anomaly and a high-resolution air-sea heat flux product for the 16-year period from 2000 to 2015, we conducted the composite patterns of air-sea fluxes and variables associated with anticyclonic eddies (AEs) and cyclonic eddies (CEs). It is found that the SST-sea surface height correlations over eddies are not always positive. Only 56% of AEs are corresponded with positive SST anomalies (SSTA), that is, SST$^+$ AEs, and 58% of CEs with negative SSTA, that is, SST$^-$ CEs. The percentage of these eddies increases with eddy amplitude and shows slight seasonal variations, higher in winter and lower in summer. Composites of SSTA, air-sea variables, and fluxes are constructed over all eddies, including both SST$^+$ eddies and SST$^-$ eddies. All composites show asymmetric patterns, showing that the centers (where the extrema are located) of the fluxes and variables shift westward and poleward (equatorward) relative to the AEs (CEs) cores. Besides, composites of latent heat flux (LHF), sensible heat flux (SHF), and air temperature show monopole patterns, while composites of wind speed and specific humidity show dipole patterns. For SST$^+$ AEs, the coupling strength is 39.6 ± 6.5 W/m^2 (7.2 ± 1.7 W/m^2) per degree increase of SSTA for LHF (SHF). For SST$^-$ CEs, the coupling strength is 39.0 ± 2.0 W/m^2 (9.0 ± 0.96 W/m^2) per degree decrease of SSTA for LHF (SHF).

1. Introduction

The South China Sea (SCS) is the largest semienclosed marginal sea of the Northwestern Pacific. It is connected to the Sulu and Java Seas by several shallow-water passages in the South and the Pacific Ocean by the deep Luzon Strait in the North. Mesoscale ocean eddies, which have spatial scales of tens to hundreds of kilometers and temporal scales of days and months, are common features in the SCS (e.g., Chen et al., 2011; Chow et al., 2008; Hwang & Chen, 2000; Jia & Liu, 2004; Liu et al., 2008; Wang, 2003; Wang, Chen, et al., 2008; Wang, Xu, et al., 2008; Wang et al., 2015; Xiu et al., 2010; Zhuang, Xie, et al., 2010). These eddies impose sufficient impacts on the thermocline structure and modify the circulation dynamics in the basin (e.g., Chen et al., 2017; Liu et al., 2001; Zhang et al., 2016). They also play an important role in oceanic transports of heat, salt, and biogeochemical properties (e.g., Chen et al., 2012, 2011; Guo et al., 2015; He et al., 2018; Xiu & Chai, 2011; Xiu et al., 2010).

Over the past decade, mounting satellite observations have shown that sea surface temperature anomalies (SSTAs) associated with mesoscale eddies induce substantial atmospheric responses, with eddy signature identifiable from near-surface wind, cloud, and precipitation (e.g., Chelton et al., 2004; Chelton & Xie, 2010; Frenger et al., 2013; Gaube et al., 2015; Hausmann & Czaja, 2012; O'Neill et al., 2010; Small et al., 2008; Song et al., 2006). Positive correlations exist between SSTA and atmospheric variables over mesoscale eddies, featuring intensified winds and increased cloud amount and rainfall over warm-core anticyclonic eddies (AEs), and weakened winds and decreased cloud amount and rainfall over cold-core cyclonic eddies (CEs) (Frenger et al., 2013; Small et al., 2008). There are also reports on the eddy imprint on surface turbulent latent heat flux (LHF) and sensible heat flux (SHF) (Bôas et al., 2015; Leyba et al., 2017; Putrasahan et al., 2017). These patterns of atmospheric responses are consistent with the vertical mixing

mechanism of Hayes et al. (1989) and Wallace et al. (1989), supporting that mesoscale eddy-induced SSTA modulates the turbulence mixing in the atmospheric marine boundary layer.

Mesoscale oceanic eddies and fronts in the SCS and their interactions with the overlying atmosphere have been studied extensively. For instance,Wang, Chen, et al. (2008) examined the oceanic effects of the orographic wind jets associated with the northeast winter monsoon along the eastern boundary of the SCS. They suggested that the wind jets through island gaps are an important generation mechanism for the rich eddy activity in the basin (Wang, 2003). Chow and Liu (2012) studied spatial variations in sea surface temperature (SST) and surface winds associated with winter warm and cold eddies in the continental slope of the northern SCS. They found that the eddy-induced SST and wind variations are spatially nonuniform, with the center of maximum response shifting southwestward with eddy motion. Sun et al. (2016) showed that there are substantial seasonal differences in spatial patterns of the eddy-induced changes in SST and wind speed. In summer, the eddy-induced SSTA show a monopole pattern, with maximum SSTA centered on the maximum sea surface height anomaly (SSHA). In winter, the eddy-induced SSTA develop into a dipole pattern, and the orientation of the dipole varies with the eddy polarity. For AEs (CEs), positive SSTA are located on the west (northeast) side and negative SSTA on the east (southwest) side. The patterns of wind speed anomalies over mesoscale eddies demonstrated similar seasonal differences to those of SSTA. Sun et al. (2016) suggested that seasonal changes of the coupling patterns are caused by seasonally reversing monsoonal winds and the associated changes in the background SST gradients. The basin-scale forcing preconditions the horizontal and vertical heat advection over eddies.

Most studies of the eddy-scale air-sea interaction have focused primarily on the response of near-surface winds to eddy SSTA. The thermal effects of ocean eddies on the marine boundary layer have gained increasing attention lately (Bôas et al., 2015; Leyba et al., 2017; Putrasahan et al., 2017). Liu et al. (2018) produced a detailed composite analysis of the coupling between ocean eddies and atmospheric anomalies using surface winds and surface LHF and SHF, precipitation, and cloud liquid water. They also performed a 7-day simulation of the atmospheric response to an eddy dipole off eastern Vietnam using a nested dynamic downscale model forced by observed SST. The model simulations show that the eddy-induced heat flux anomalies affect the atmospheric stability and hence buoyancy, and the latter modulates vertical mixing (Hayes et al., 1989; Wallace et al., 1989). Enhanced (reduced) turbulent mixing over a warm (cold) eddy increases (decreases) downward momentum transfer, resulting in an acceleration (deceleration) of surface winds over the eddy. Meanwhile, Liu et al. (2018) cautioned about the coupling strength derived from the satellite-based data sets, as they found that the magnitude of the eddy-induced atmospheric anomalies is comparable to the magnitude of the errors in data sets. The flux data sets used in their quantification were the daily turbulent LHF and SHF data sets on 1° grids from the Objectively Analyzed air-sea Fluxes (OAFlux) (Yu et al., 2008; Yu & Weller, 2007) and the 3-day averaged precipitation and water vapor data sets from Remote System Systems (Hilburn & Wentz, 2008). These data sets are not ideal because the spatial and temporal resolution may not be sufficient for resolving mesoscale eddies.

The present study aims to use the newly developed 0.25° gridded satellite-derived LHF and SHF products (Yu, 2019; Yu & Jin, 2014, 2018) to quantify and characterize the atmospheric thermal response to oceanic eddies via LHF and SHF. The study focuses on developing a statistical characterization of two main mesoscale features: the pattern and magnitude of LHF and SHF anomalies associated with the eddy-induced SSTA in the SCS. However, during the course of the study, the issue at the heart of finding the coupling between the atmosphere and ocean eddies is the sign of the SSTA over eddies. It is conventionally believed that the AEs are associated with positive SSTA, and conversely, the CEs are with negative SSTA. We found that this concept does not hold everywhere for the mesoscale eddies in the SCS. We also found that the SCS is not the only region where SSTA can be out of phase with SSHA over some eddies. Similar feature has been identified in the Tasmania Sea (a marginal sea of the South Pacific Ocean) by Everett et al. (2012), in the Southwestern Atlantic by Leyba et al. (2017), and also in the North Pacific by Sun et al. (2019). Since SSTA are the link between ocean eddies and the overlying atmosphere, a good understanding of the relationship between SSHA and SSTA over eddies is the prerequisite for the understanding of the air-sea coupling on eddy scales. Therefore, this study has three specific objectives: (i) to produce an eddy climatology for the period of 2000–2015 using an eddy detection and tracking approach with computational efficiency (section 3.1), (ii) to provide a statistical characterization of spatiotemporal variations of mesoscale eddies (section 3.2), and

(iii) to determine the pattern and strength of LHF and SHF in response to mesoscale eddies (section 3.3). A summary is included in section 4.

2. Data and Methods

2.1. Data

Three sets of satellite-derived products are used in the study, including sea surface height (SSH), SST, LHF, and SHF. A brief description of each data set is given below.

The SSH product is produced by Ssalto/Duacs and distributed by the Archiving, Validation, and Interpretation of Satellite Oceanographic (AVISO) and is available daily on 0.25° spatial resolution. The product is merged from all available altimeter missions, including TOPEX/Poseidon, Jason-1 and Jason-2, European Remote Sensing Satellite (ERS)-1 and 2, Environmental Satellite, Geosat Follow On, Cryosat-2, Saral/AltiKa, and Haiyang-2A, and covers the period from 1993 to the present. Since resolving ocean mesoscale variability requires a minimum of three altimeter missions (Le Traon & Dibarboure, 1999; Pascual et al., 2007; Pujol et al., 2016), only the period from 2000 onward meets the criterion. The 16-year period from 2000 to 2015 is therefore selected. Ducet et al. (2000) showed that the product has a nominal uncertainty of 2 cm, which is sufficient for resolving mesoscale eddy structures that have a diameter of 70 km and larger.

The SST data set is the National Oceanic and Atmospheric Administration Optimum Interpolation SST product from Reynolds et al. (2007) on daily and 0.25° resolution. The Optimum Interpolation SST data set is constructed from infrared satellite observations of the Advanced Very High Resolution Radiometer with supplemental information provided by in situ observations and proxy SSTs computed from sea ice concentrations. Error fields were provided, showing an accuracy of about 0.1 °C on daily basis. The Optimum Interpolation SST data set is available from 1981 onward. The period of 2000–2015 is used to be consistent with the eddy-resolving period permitted by the AVISO SSHA data set.

The data sets of LHF and SHF and related surface meteorological variables are from the newly developed high-resolution satellite-derived analysis by the OAFlux project (Yu, 2019; Yu & Jin, 2014, 2018). Compared to the 1° gridded OAFlux analysis (Yu & Weller, 2007), the 0.25° gridded OAFlux-HR analysis has made two major improvements. The first is that near-surface air temperature and specific humidity are retrieved from 11 satellite sensors, including microwave passive radiometers and sounders (Yu & Jin, 2018). It is different from the 1° gridded OAFlux that is obtained from objective synthesis of the output from atmospheric reanalyses. The second improvement is that wind speed and direction are derived simultaneously from 16 satellite sensors including scatterometers and microwave passive radiometers (Yu & Jin, 2014). By comparison, the OAFlux-1° analysis has wind speed but no wind direction.

The LHF and SHF of OAFlux-HR are computed from the COARE bulk flux algorithm (Fairall et al., 2003) using surface meteorological variables that are all derived from satellites. The bulk flux parameterizations for LHF and SHF are expressed as follows:

$$\mathrm{LHF} = \rho L_e c_e U(q_s - q_a) \tag{1}$$

$$\mathrm{SHF} = \rho c_p c_h U(T_s - T_a) \tag{2}$$

where ρ is air density and L_e is the latent heat of vaporization and is a function of SST (T_s), expressed as $L_e = (2.501 - 0.00237 \times T_s) \times 1.0^6$. c_p is the specific heat capacity of air at constant pressure, and c_e and c_h are the stability- and height-dependent turbulent exchange coefficients for latent and sensible heat, respectively. T_a and q_a are the air temperature and specific humidity at the reference height of 2 m above the sea surface. U is the wind speed at the reference height of 10 m. q_s is the saturation humidity at T_s.

2.2. Eddy Identification and Tracking

Several automated eddy detection methods have been proposed to identify mesoscale eddies automatically. These methods can be categorized into the three types: the physical parameter-based methods that utilize the physical characteristics (i.e., vorticity) of the flow field (Chaigneau et al., 2008; Doglioli et al., 2007; Isern-Fontanet et al., 2003), the flow geometry-based methods that identify eddies based on the shape or curvature of the streamlines (Nencioli et al., 2010), and the SSH-based methods (Chelton et al., 2011; Faghmous

et al., 2015) that identify eddies by finding closed contours of SSH encircling a set of grid points. This study used the SSH-based approach and implemented a parallel computation to improve the computational processing speed and efficiency (Liu et al., 2016).

Details of the eddy detection are given as follows. A spatially high pass filter with half-power filter cutoffs of 20° in longitude and 10 ° in latitude was first applied to AVISO SSHA map. The potential CE (AE) core was then searched by identifying local minimum (or maximum) in the SSHA map. The search used the threshold that defines the minimum (maximum) to be the pixel whose value is lower (higher) than its eight neighboring pixels in a 3 × 3 neighborhood. Once selected, the SSHA contours were computed from minimum (maximum) SSHA values to maximum (minimum) SSHA values at 0.25-cm intervals. The following five criteria were applied to determine whether an eddy could be established (Liu et al., 2016): (1) The SSHA contours contain no more than one local maxima/minima. (2) The SSHA contours are located in areas where water depths are greater than 200 m to minimize the impacts of data errors near the coastal shallow water region (Cheng & Qi, 2010). (3) The shape error of eddy (Cheng et al., 2014; Kurian et al., 2011), denoted $Error_{shape}$, does not exceed 55%, where $Error_{shape} = Area_{deviation}/Area_{circle} \times 100\%$, with $Area_{circle}$ being the area of a fitted ideal circle, and $Area_{deviation}$ the difference between the area closed by SSHA contours and the area closed by the fitted ideal circle. (4) The eddy has a radius larger than 35 km, as the SSHA data set is filtered with cutoff wavelength of 25–35 km (Morrow et al., 2017). (5) The eddy amplitude, defined as the SSHA differences between the eddy core and the eddy boundary, needs to be greater than the SSHA data precision of 2 cm. An eddy is selected once the closed SSHA contours satisfy all these five criteria. The seed inside the eddy is defined as the eddy center, and the outermost closed SSHA contour is referred to as the effective perimeter of the eddy (C_{eff}). Following Chelton et al. (2011), the region within a closed SSHA contour that has the maximum average geostrophic speed (C_{spd}) is regarded as the more robust property of an eddy. Therefore, C_{spd} is used to define the boundary of the eddy, which is estimated by iterating C_{eff} inward over all closed SSHA contours. The eddy radius is defined as the radius of the circle that has the same area as the region within the C_{spd}.

An automated eddy-tracking procedure was used to track the eddy by comparing eddy centers and properties at consecutive time levels. For a given eddy (e_1) that is identified at time step t_1, the eddy at the subsequent time step t_2 is searched by finding the closest eddy that lies within the predefined search region. The searching distance, D, is set to 1.75 times the distance that a long baroclinic Rossby wave would propagate in 1-day time step. If an eddy at time step t_2 is located within the searching distance and has the amplitude and size within 0.25–2.75 times of those of eddy e_1, then the eddy is regarded as eddy e_1. The use of a large range of amplitude and size in defining the eddy screening criteria is intended not only to accommodate noise in the SSH fields (Chelton et al., 2011) but also to take into account the changes due to merging or splitting of eddies. In case more than one eddy passes the above-mentioned tests, the nearest one is selected. Since eddies may disappear between consecutive maps due to the sampling errors or measurement noise, eddies are allowed to be unassociated for one day before the track is terminated. If no eddies are found, the track of e_1 is terminated, and a new eddy track is initiated.

2.3. Identification of Eddy Signature in Air-Sea Variables and Fluxes

To identify eddy-induced mesoscale features in air-sea variables and fluxes (e.g., SST, LHF, SHF, and flux-related surface meteorology), the temporal and spatial filters similar to those used in Bôas et al. (2015) were applied to all related air-sea variables and fluxes fields. The temporal filter was a band-pass Butterworth window designed to retain the temporal signal between 7 and 90 days. The spatial filter was a moving average Hann window, which was used to retain spatial scales smaller than 600 km. Eddy-induced anomalies in air-sea variables and fluxes were then used to construct composite maps over mesoscale eddies. For each identified eddy with a radius of R, the potential eddy-induced anomalies were searched in a circular area of $2R$ surrounding the eddy core and interpolated onto a uniform grid that was normalized by R. The composite maps of eddy-induced anomalies were produced by averaging anomaly fields over all AEs and CEs, respectively.

Table 1
Eddy Amplitude, Mean Radius, Mean Lifetime, and Eddy Number at Four Amplitude Percentiles

Percentile	Amplitude (cm)	Mean radius (km)	Mean lifetime (days)	Number	
				AEs	CEs
0th to 55th	2–4.4	62.4	60	15,771	16,653
55th to 85th	4.4–7.4	77.1	72	8,041	9,669
85th to 95th	7.4–10.2	92.3	82	2,956	2,953
95th to 100th	10.2–26.4	107.1	91	1,841	1,106

3. Results and Discussion

3.1. Mesoscale Eddy Climatology (2000–2015) in the SCS

Following the eddy identification procedure described in section 2.2, eddies were isolated and tracked using daily SSHA fields from 2000 to 2015. To avoid sporadic events, eddies with a duration shorter than 28 days were excluded. This led to a total of 28,609 AEs and 30,381 CEs for the 16-year analysis period. In the literature, some studies examined only large eddies, that is, the eddies with amplitude no less than the 95th amplitude percentile (e.g., Bôas et al., 2015), while other studies included eddies at all amplitudes (e.g., Chen et al., 2011; Liu et al., 2018). In this study, eddies were divided into four amplitude percentile intervals, 0th to 55th (2–4.4 cm), 55th to 85th (4.4–7.4 cm), 85–95th (7.4–10.2 cm), and 95–100th (10.2–26.4 cm) percentiles, to examine the sensitivity of the eddy-induced air-sea response to eddy amplitude. Major characteristics of these eddies, including the eddy number for AEs and CEs, the C_{spd}-based eddy radius, the eddy amplitude, and the duration of 28 days and longer, are summarized according to amplitude percentile at four intervals (Table 1). One noted feature is that the number of AEs is generally less than that of CEs for eddy amplitudes less than 85th percentile, but the situation reverses for eddy amplitude greater than 85th. Overall, for larger and longer-lasting eddies in the SCS, there are more AEs than CEs, although the total number of AEs at all amplitudes is less than that of CEs. Distributions of the number of AEs (red color) and CEs (blue color) across the continuous ranges of amplitude, radius, and duration are summarized in Figures 1a–1c.

The 28,609 AE realizations correspond to 1,106 AE trajectories, and the 30,381 CE realizations correspond to 1,167 CE trajectories. The spatial distribution of the eddy initial positions (birth locations) and the subsequent trajectories (colored by eddy lifespan) are shown in Figure 2. Mesoscale eddies are ubiquitous in the SCS, but one feature is clearly seen: Eddies with shorter lifetimes (<9 weeks) are randomly distributed, while eddies with longer lifetimes tend to cluster together along a few preferred corridors. In the northern basin, the eddies have a southwestward migration pathway that extends from the west of the Luzon Strait to the southeast of Hainan Island along the continental shelf. In the central basin, both CEs and AEs propagate westward. In the southern SCS, a southwestward migration pathway is featured by both CEs and AEs, but the CEs along this pathway have longer durations. These eddy propagation pathways are basically consistent with previous findings (Chen et al., 2011; Du et al., 2016; Wang, 2003; Xiu et al., 2010; Zhuang, Du, et al., 2010).

3.2. Relationship Between SSTA and SSHA Over Mesoscale Eddies

3.2.1. Case Analysis of Eddy SSTA Along Eddy Trajectories

It is conventionally believed that the AEs are associated with positive SSTA, and the CEs are with negative SSTA. However, this concept does not always hold in the SCS. This is observed following the evolution of eddy-induced SSTA along two eddy trajectories, one for AE and the other for CE (Figure 3a). The SSTA values were the averages of the SSTA within one eddy radius. The AE trajectory started from the west of the Luzon Strait near 20°N, 120°E on 19 November 2009 and extended southwestward along the continental shelf until its termination near 17°N, 110°E after 275 days. The CE trajectory originated on 9 January 2009 at a location about 4° of latitude further south than the AE trajectory and extended westward across the basin to about 17°N, 113°E after 215 days.

The eddy amplitude and associated SSTA along the AE and CE trajectories (Figures 3b and 3c) both have an interesting feature: The SSTA along the eddy migration pathway changed signs frequently. SSTA could be either positive or negative over the AEs, and so were SSTA over the CEs. During the lifetime of the AE, the occurrence of positive SSTA accounts for only 54% (49%) of the time. Since SSTA is a key parameter in coupling the atmosphere to ocean eddies, the sign between SSTA and eddies is important for understanding the eddy-induced atmospheric responses. In the study, AEs associated with positive SSTA and negative SSTA are defined as SST^+ AEs and SST^- AEs, respectively. Besides, CEs associated with negative SSTA, and CEs associated with positive SSTA are defined as SST^- CEs and SST^+ CEs, respectively.

3.2.2. Distribution of SSTA Over Mesoscale Eddies

There are 16,038 SST^+ AEs out of 28,609 AE realizations and 17,700 SST^- CEs out of 30,381 CE realizations. Hence, about 56% of AEs are SST^+ AEs and 58% of CEs are SST^- CEs. The sign inconsistency

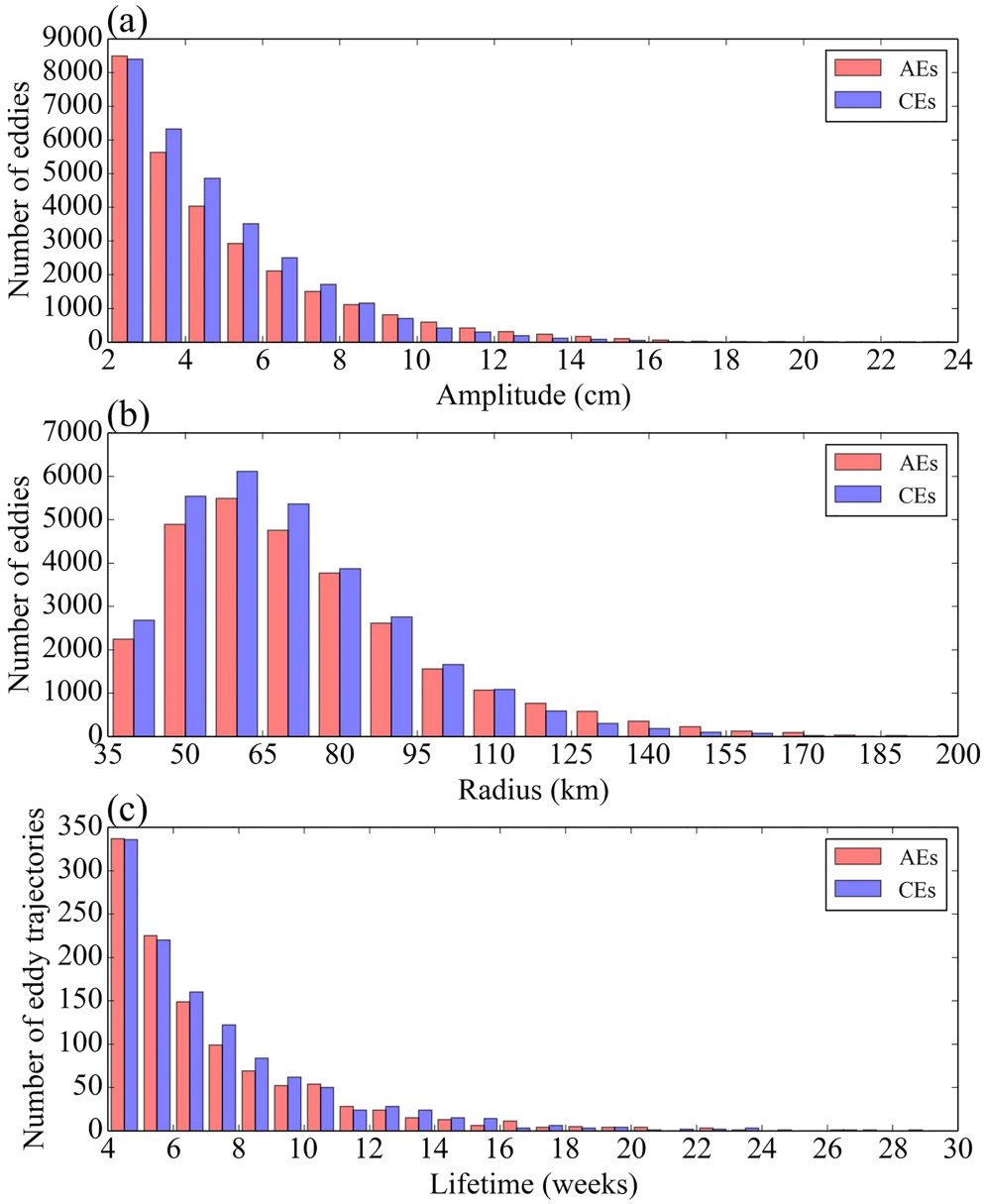

Figure 1. Histogram of (a) eddy amplitude, (b) eddy radius, and (c) eddy lifetime constructed for the 2000–2015 period. Red and blue bars stand for AEs and CEs, respectively.

between SSTA and SSHA has been found in other world basins (e.g., Chaigneau et al., 2011; Everett et al., 2012; Leyba et al., 2017; Sun et al., 2019). Spatial distributions of AEs associated with all ranges of SSTA, SST^+ AEs, and the percentage between the two sets of eddies are shown in Figures 4a–4d, respectively. Similar spatial patterns are also constructed for CEs (Figures 5a–5d). To see whether the relationship between SSHA and SSTA is dependent on eddy amplitude, the patterns are shown for all four amplitude percentiles. Two features are worth noting. First, SST^- AEs occurred at all ranges of eddy amplitude, and so did SST^+ CEs. The sign inconsistency between SSTA and the eddy core is a ubiquitous feature in the SCS. Second, the percentage of SST^+ AEs and SST^- CEs relative to the respective total eddies increases slightly with eddy amplitude. For AEs, the percentage increases from 54% at the 0th to 55th amplitude percentile to 62% at the 95th to 100th percentile. For CEs, the percentage goes from 55% to 68% at the low and high ends of amplitude percentile. Seasonal variations of the number of these eddies show a slight change with seasons (Figure 6), increasing from ~ 50% in

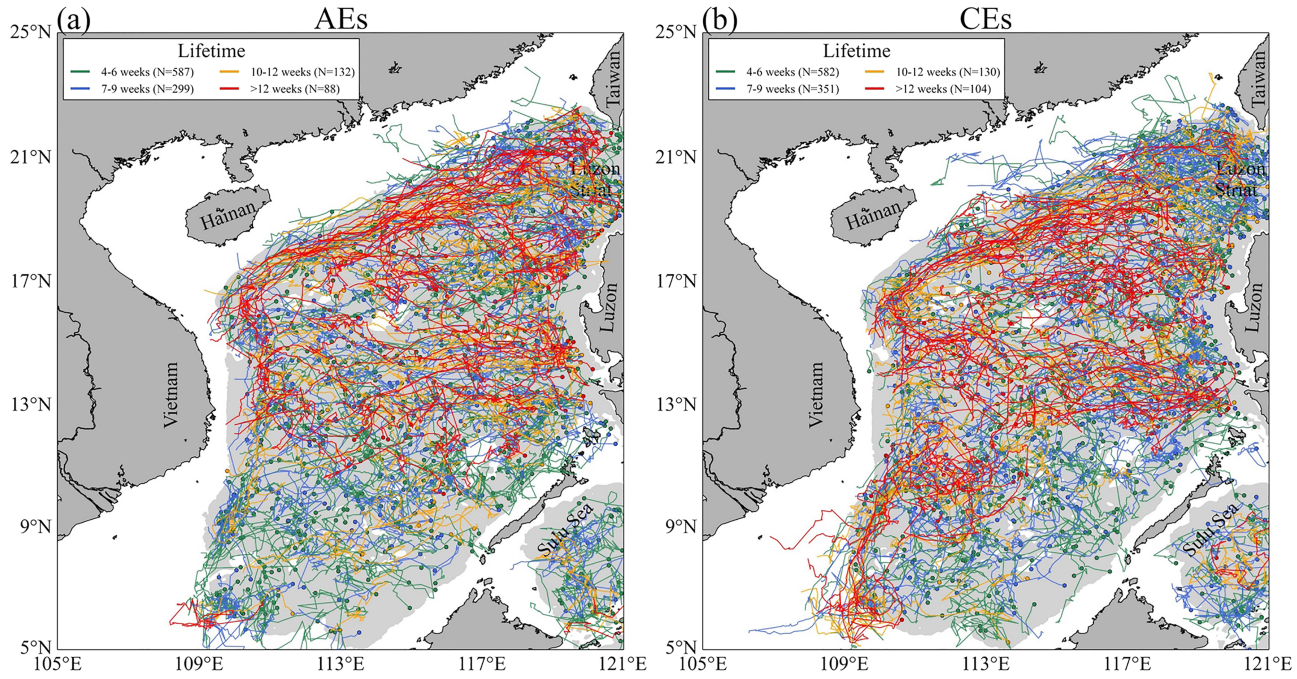

Figure 2. Eddy trajectories for (a) AEs and (b) CEs. Dots denote birth positions of eddies and lines the propagation pathways, color coded based on lifetime. Eddies with longer lifespans are plotted on top of the eddies with shorter lifespans. Gray shading denotes the seabed area with water depth greater than 200 m.

the summer monsoon months (April–September) to above 60% in the winter monsoon months (October–March), for both cases of AEs and CEs.

Several factors are proposed to result in the sign inconsistency between SSTA and SSHA associated with mesoscale eddies. Everett et al. (2012) found that about 22% of AEs are SST^- AEs, and 44% of CEs are SST^+ CEs in the Tasmania Sea. They suggested that these eddies may be induced by two reasons. First,

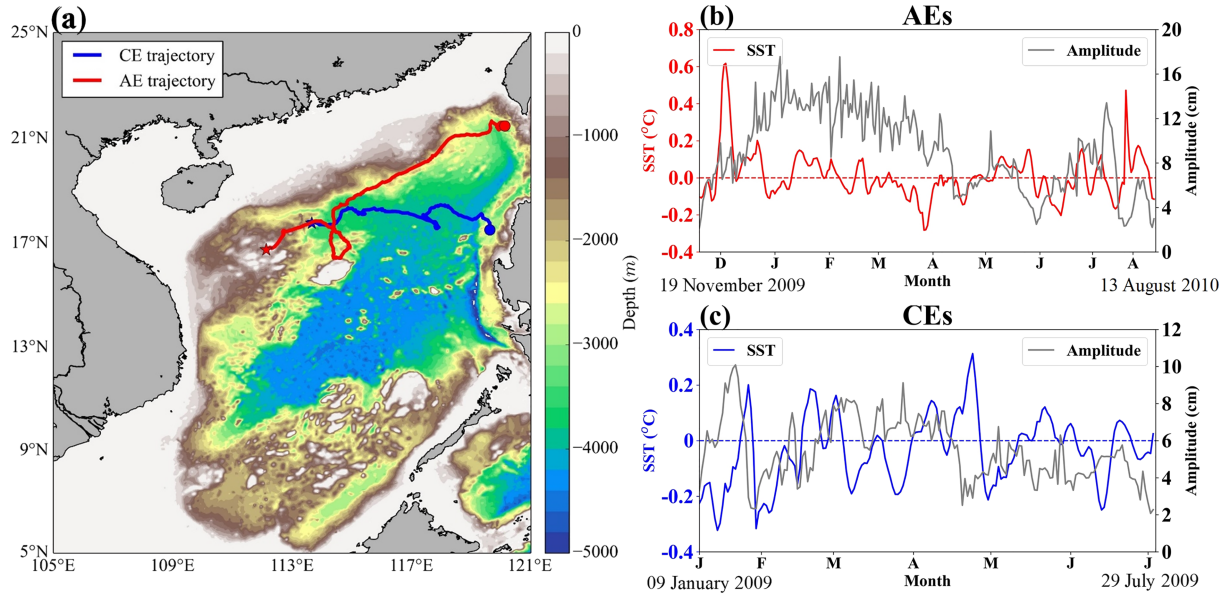

Figure 3. (a) Two eddy trajectories in the SCS. The AE trajectory (red) has a lifetime of 275 days, and the CE trajectory (blue) has a lifetime of 215 days. Dots and stars denote the generation and termination locations, respectively. (b) SSTA (red) along the AE trajectory, and c SSTA (blue) along the CE trajectory. The eddy amplitude (gray) is shown in both (b) and (c).

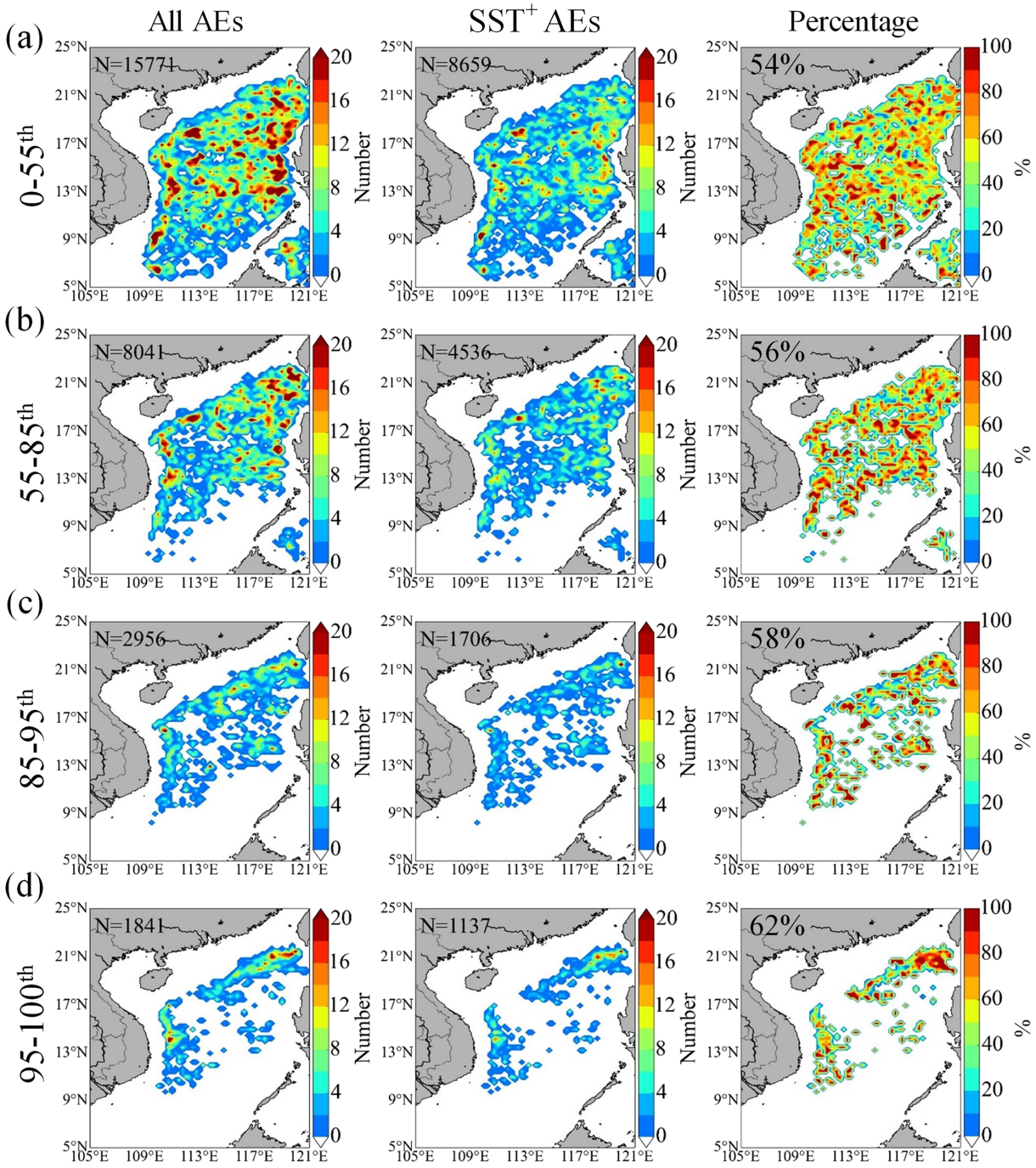

Figure 4. Spatial distribution of eddy centroids for (left) all AEs, (middle) SST^+ AEs, and (right) percentage of SST^+ AEs relative to the total AEs that fall at the amplitude percentiles of (a) 0th to 55th, (b) 55th to 85th, (c) 85th to 95th, and (d) 95th to 100th. *N* is the total number of eddy realizations that are constructed from daily, 0.25° × 0.25° binned fields.

because of errors in estimating the center of noncircular eddies in the census and second due to surface anomalies such as surface flooding or mixing, not reflecting the underlying eddy properties. For instance, surface heating or flows of warm water can result in positive SSTA over CEs, and wind-induced upwelling may induce negative SSTA over AEs. Leyba et al. (2017) found some CEs are associated with positive heat anomalies in the Brazil-Malvinas Confluence and considered to be induced by the location of eddy formation. These CEs come from the north transport subtropical waters, which are very warm. Hence, they are

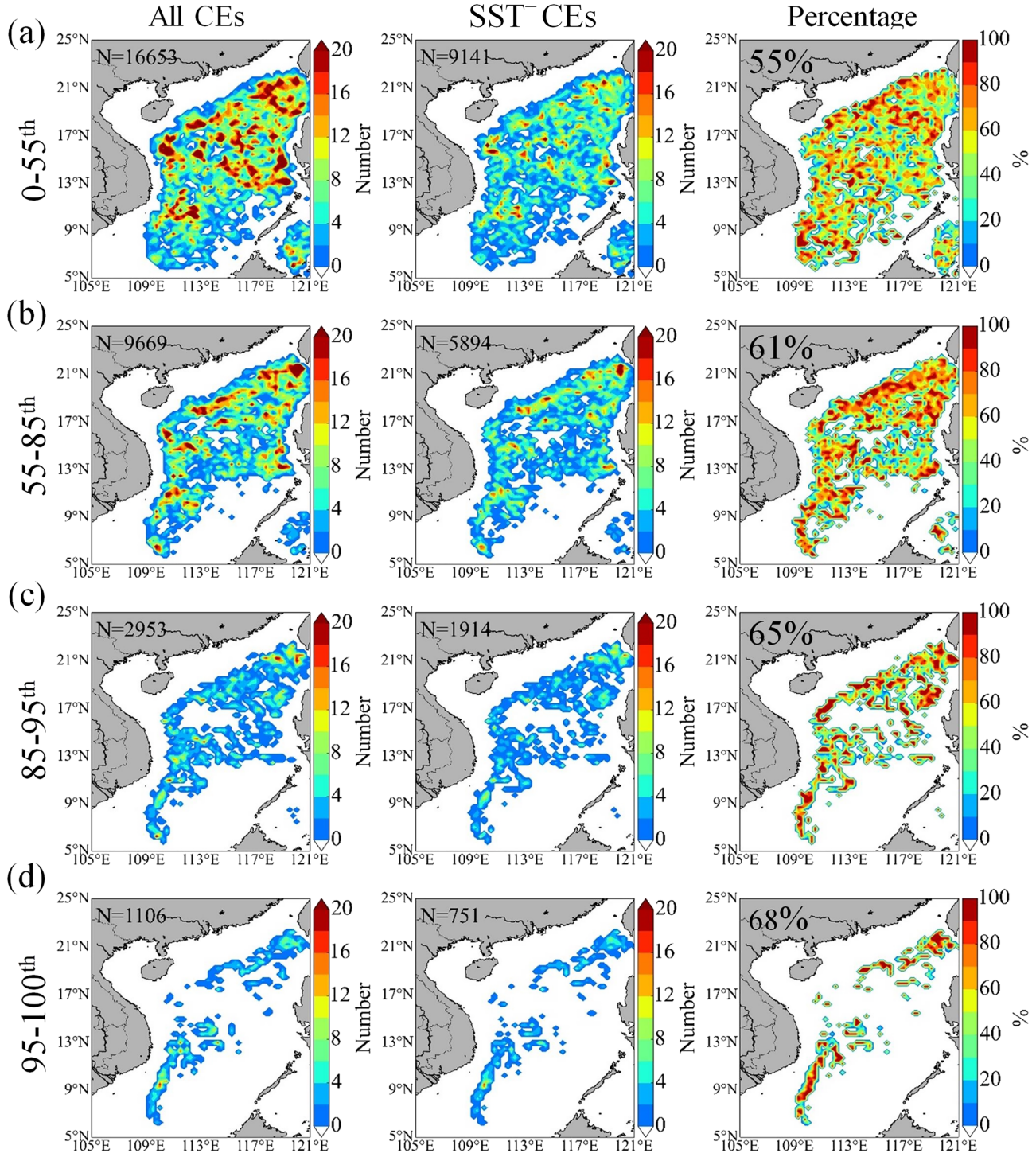

Figure 5. Same as Figure 4 but for (left) all CEs, (middle) SST^- CEs, and (right) percentage of SST^- CEs relative to the total CEs.

not enough to cool surface warm waters and thus result in positive SSTA at the surface. Sun et al. (2019) studied the warm-core CEs (i.e., SST^+ CEs) and cold-core AEs (i.e., SST^- AEs) in the North Pacific. They suggested that the instability during the eddy decay stage and eddy horizontal entrainment may induce the negative correlated SSTA at the surface within eddies. The reasons proposed by previous literature may lead to the negative SSHA-SSTA correlation within eddies in the SCS. However, exploring the

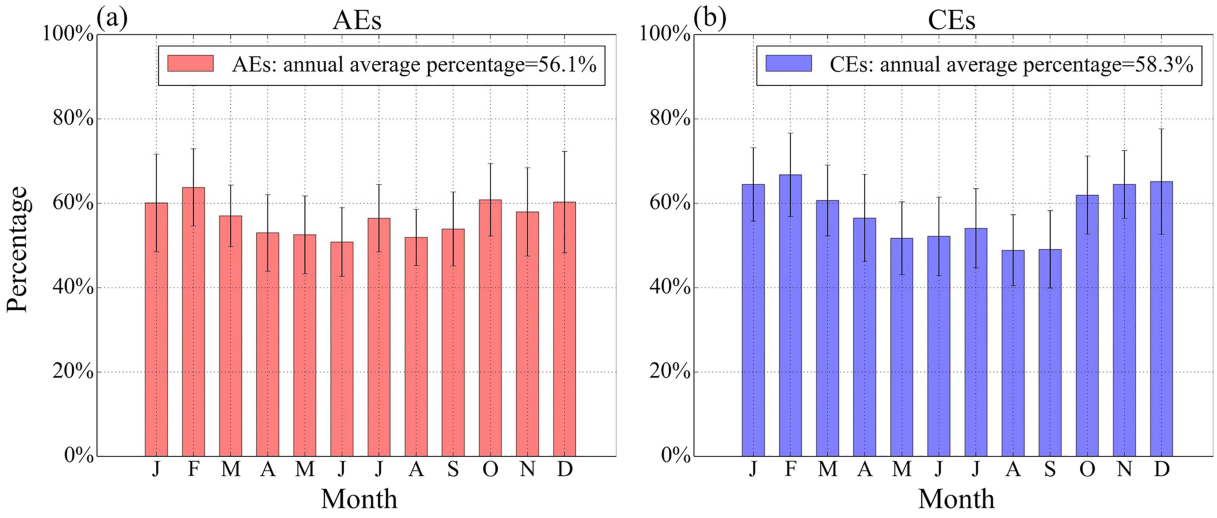

Figure 6. Seasonal distribution of the percentage of (a) SST^+ AEs and (b) SST^- CEs relative to the respective total AEs and CEs. Error bars represent the ±1 standard deviation of monthly values. The annual average percentage is the average of all 12 months.

underlying mechanisms for those nonconventional eddies are beyond the scope of this work and deserve future study.

3.2.3. SSTA Composites Over Mesoscale Eddies

To examine the dependence of the composite SSTA patterns to eddy amplitude, composite SSTA over AEs, and CEs at all four amplitude percentiles are constructed in Figures 7 and 8, respectively. All three cases are considered, including all eddies, SST^+ eddies, and SST^- eddies. Differences in the SSTA composite patterns at the four amplitude percentiles are small, except that the spatial structure tends to be fuller and more rounded toward the lower percentiles. The latter may be related to the number of eddy realizations used in making the composite average. For instance, there are 15,771 AE realizations at the 0th to 55th percentile but only 1,841 AE realization at the 95th to 100th percentile.

When constructed over all AEs (Figure 7a), the SSTA composites are positive and smaller than those constructed over the SST^+ AEs (Figure 7b). Conversely, SSTA composites constructed over SST^- AEs are negative (Figure 7c). Except for the opposite sign of SSTA, the similar finding can be seen for CEs (Figure 8). It is worth noting that the eddy-induced SSTA are not collocated with the SSHA-based eddy centers for both AEs and CEs. The SSTA composites show an asymmetric monopole pattern over eddies. Extrema of SSTA composites over all AEs, SST^+ AEs, and SST^+ CEs are basically shifted westward and poleward relative to the SSHA-based eddy centers, whereas extrema of SSTA composites over all CEs, SST^- CEs, and SST^- AEs are basically shifted westward and equatorward relative to the SSHA-based eddy centers. Similar meridional and zonal phase shifts were observed in previous literature (Bôas et al., 2015; Hausmann & Czaja, 2012).

To further quantify the relationship between SSHA and SSTA associated with mesoscale eddies, the SSTA extreme within one eddy radius was obtained for each eddy realization and then binned into SSHA intervals of every 2 cm (Figure 9). Using the least squares estimation, the linear relationship between SSHA and SSTA over all eddies (Figure 9a) is clear, and so did SST^+ AEs and SST^- CEs (Figure 9b). With every 1-cm increase in SSHA, SSTA within either all AEs (all CEs) or SST^+ AEs (SST^- CEs) increases (decreases) 0.02 °C, which is stronger than the coupling between SSHA and SSTA over SST^- AEs and SST^+ CEs. As shown in Figure 9c, SSTA increases (decreases) 0.01 °C with every 1-cm increase in SSHA.

3.3. Near-Surface Atmospheric Responses to Mesoscale Eddies

3.3.1. Composites of Air-Sea Heat Fluxes and Flux-Related Variables Over Mesoscale Eddies

Since the composite SSTA patterns over either AEs or CEs are consistent at all eddy amplitude percentiles, the composites of air-sea heat fluxes and flux-related variables are constructed over all amplitude percentiles in the following analysis (Figure 10). As expected, positive SSTA destabilize the marine boundary layer, which leads to enhanced turbulent heat exchanges. Conversely, negative SSTA stabilize the marine

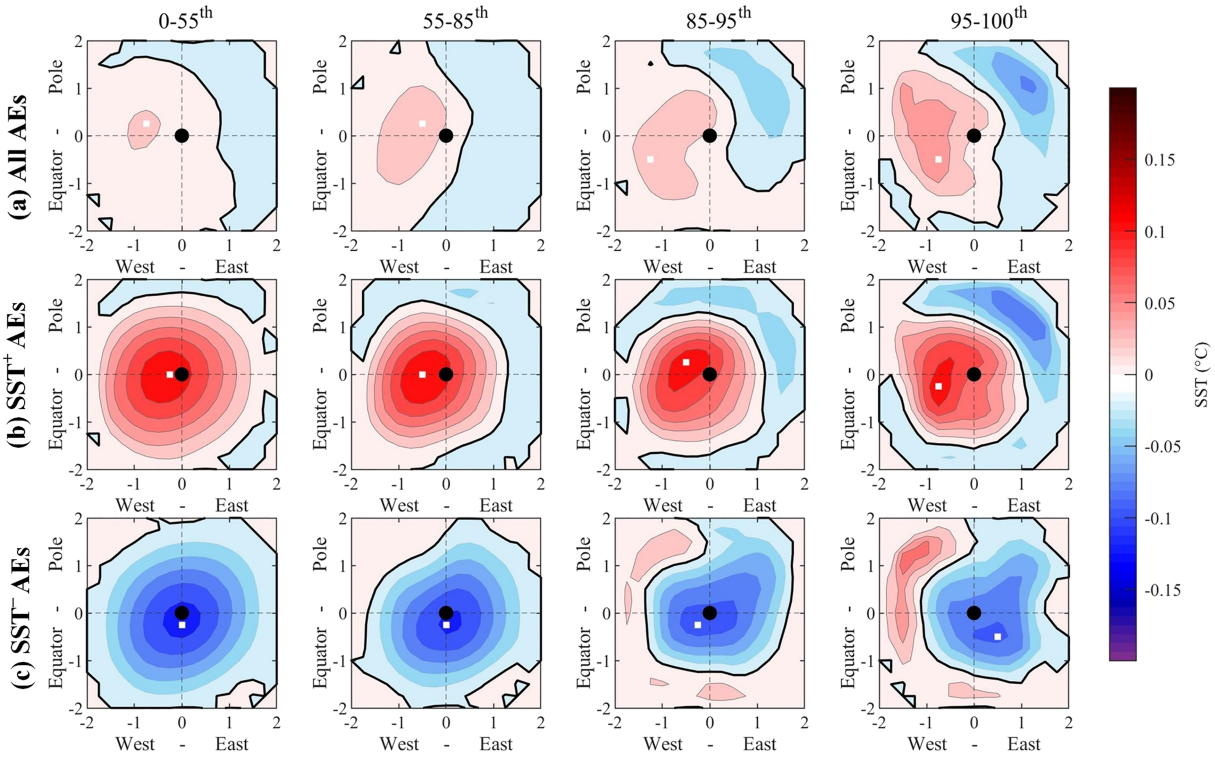

Figure 7. SSTA composites over (a) all AEs, (b) SST^+ AEs and (c) SST^- AEs at four amplitude percentiles. The axes in the composite maps are the normalized distance between the eddy center and two eddy radii. On each map, a black dot denotes the eddy center, and a white dot denotes the location of the SST maximum.

boundary layer and suppress turbulent heat exchanges (Bôas et al., 2015; Leyba et al., 2017; Putrasahan et al., 2017). The spatial patterns of composite LHF and SHF over eddies are similar to SSTA, which show an asymmetric monopole pattern. Besides, composites of LHF and SHF are positive over all AEs, SST^+ AEs, and SST^+ CEs, while negative over all CEs, SST^- AEs, and SST^- CEs.

Compared to composite SSTA, composite U over mesoscale eddies shows an asymmetric dipole pattern. Furthermore, composite U is positive over SST^-AEs and negative over SST^+ CEs. It indicates a negative correlation between SSTA and U over these eddies. Such a result differs from the previous finding that SST and U are positively correlated on oceanic mesoscales (Chelton & Xie, 2010; Small et al., 2008; Xie, 2004). Composites of other flux-related variables show similar spatial patterns and same sign with SSTA, except that composite q_a shows a dipole pattern.

Although the spatial patterns of LHF, SHF, and flux-related variables are similar to SSTA over mesoscale eddies, the locations of extrema relative to the eddy center are different. Since air-sea coupling over SST^- AEs and SST^+ CEs are more likely to be affected by other ocean phenomena (Everett et al., 2012; Leyba et al., 2017; Sun et al., 2019), only SST^+ AEs and SST^- CEs are considered in the following analysis (Figure 11). With respect to the eddy center of AEs, extrema of LHF, SHF, and U shifted westward and poleward, while extrema of SSTA and other flux-related variables shifted westward. With respect to the eddy center of CEs, the extrema of SSTA, $q_s - q_a$, $T_s - T_a$, and T_a shifted equatorward, the extrema of LHF, SHF, and q_a shifted westward and equatorward, and the extremum of U anomalies shifted westward. The values and locations of these extrema relative to the eddy centers are summarized in Table 2. The SSTA maximum of 0.11 °C within SST^+ AEs corresponds with the flux maximum of 4.07 W/m^2 for LHF and 0.67 W/m^2 for SHF and 0.02 m/s for U. Furthermore, SSTA minimum of −0.14 °C within SST^- CEs corresponds with flux minimum of −5.17 W/m^2 for LHF, −0.85 W/m^2 for SHF, and −0.04 m/s for U.

3.3.2. Air-Sea Coupling Associated With Mesoscale Eddies

Based on the 16,038 SST^+ AEs and 17,700 SST^- CEs averaged for the composite analysis, the coupling strength between extremum anomalies of SST, LHF, SHF, and flux-related variables within one eddy

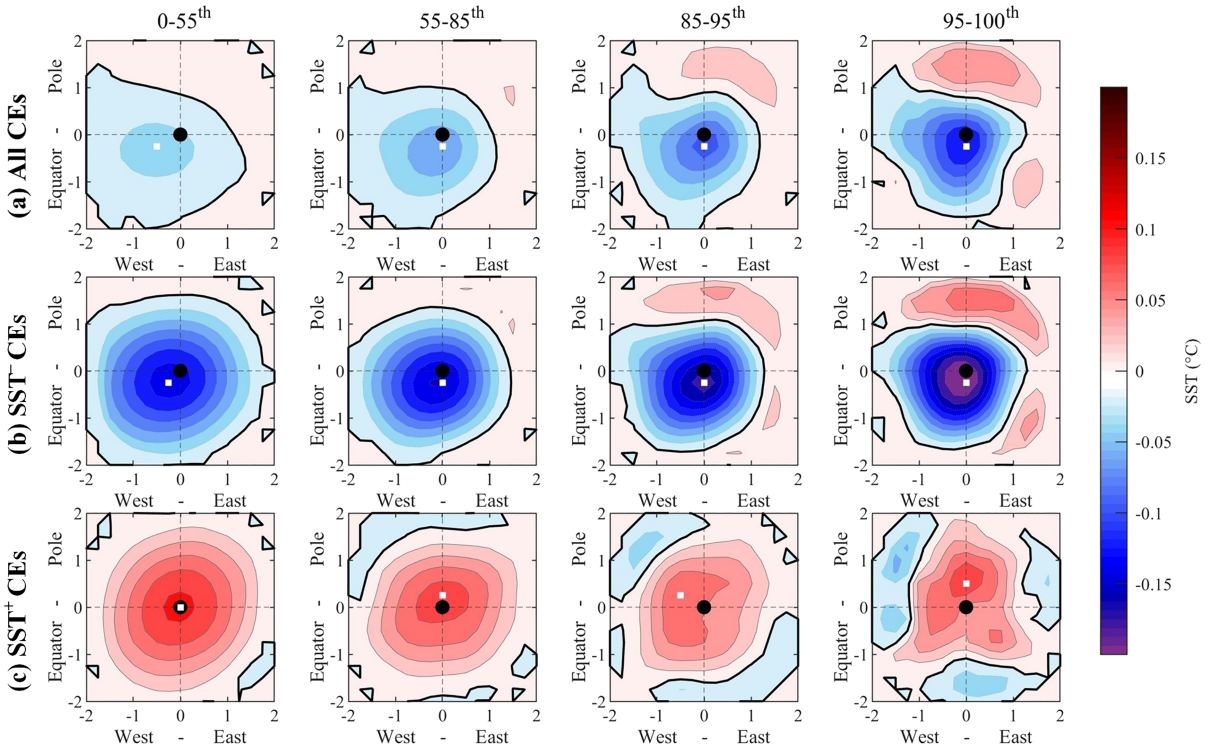

Figure 8. Same as Figure 7 but for CEs.

radius are binned onto SSTA intervals of every 0.05 °C (Figure 12). Least squares fitting was performed. There are positive linear relationships between SSTA and LHF, SHF for both AEs and CEs. As shown in Figures 12a and 12b, the coupling strength between SSTA and LHF (SHF) is 39.6 ± 6.5 W/m^2 (7.2 ± 1.7 W/m^2) per degree increase of SST over AEs, and 39.0 ± 2.0 W/m^2 (9.0 ± 0.96 W/m^2) per degree decrease of SST over CEs. The magnitude of the coupling strength between SSTA and LHF, SHF over mesoscale eddies, is similar to the result of Ma et al. (2016), which gives an approximately 40–56 W/m^2 heat flux increase per degree increase of SST.

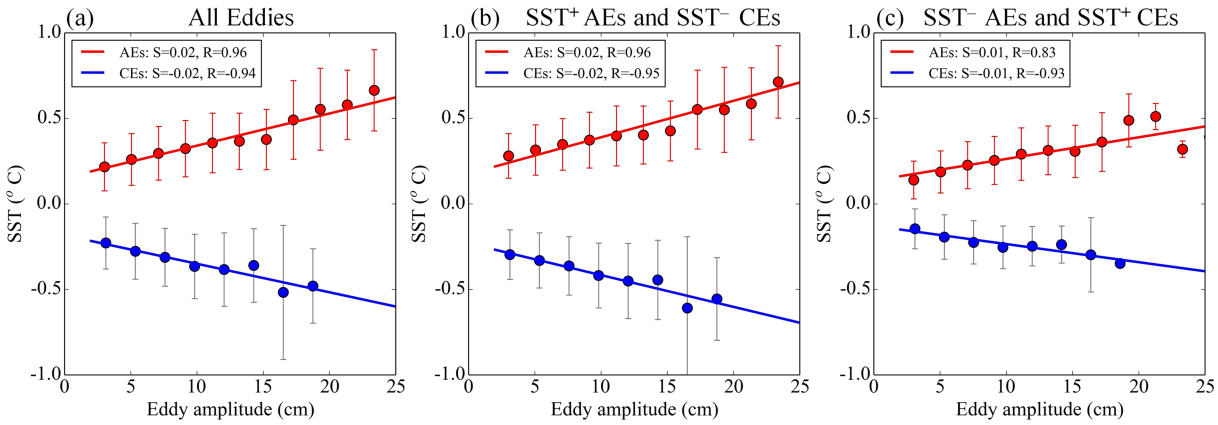

Figure 9. Extreme SSTA averaged within one radius of (a) all eddies, (b) SST$^+$ AEs and SST$^-$ CEs, and (c) SST$^-$ AEs and SST$^+$ CEs as a function of the respective eddy amplitude. Dots denote the SSTA averaged at binned SSHA intervals of 2 cm, and error bars represent the ±1 standard deviation of the samples within the SSHA bin intervals. *S* and *R* are the regression slope and correlation coefficient obtained from the least squares fitting. The values are significant at the 95% confidence level.

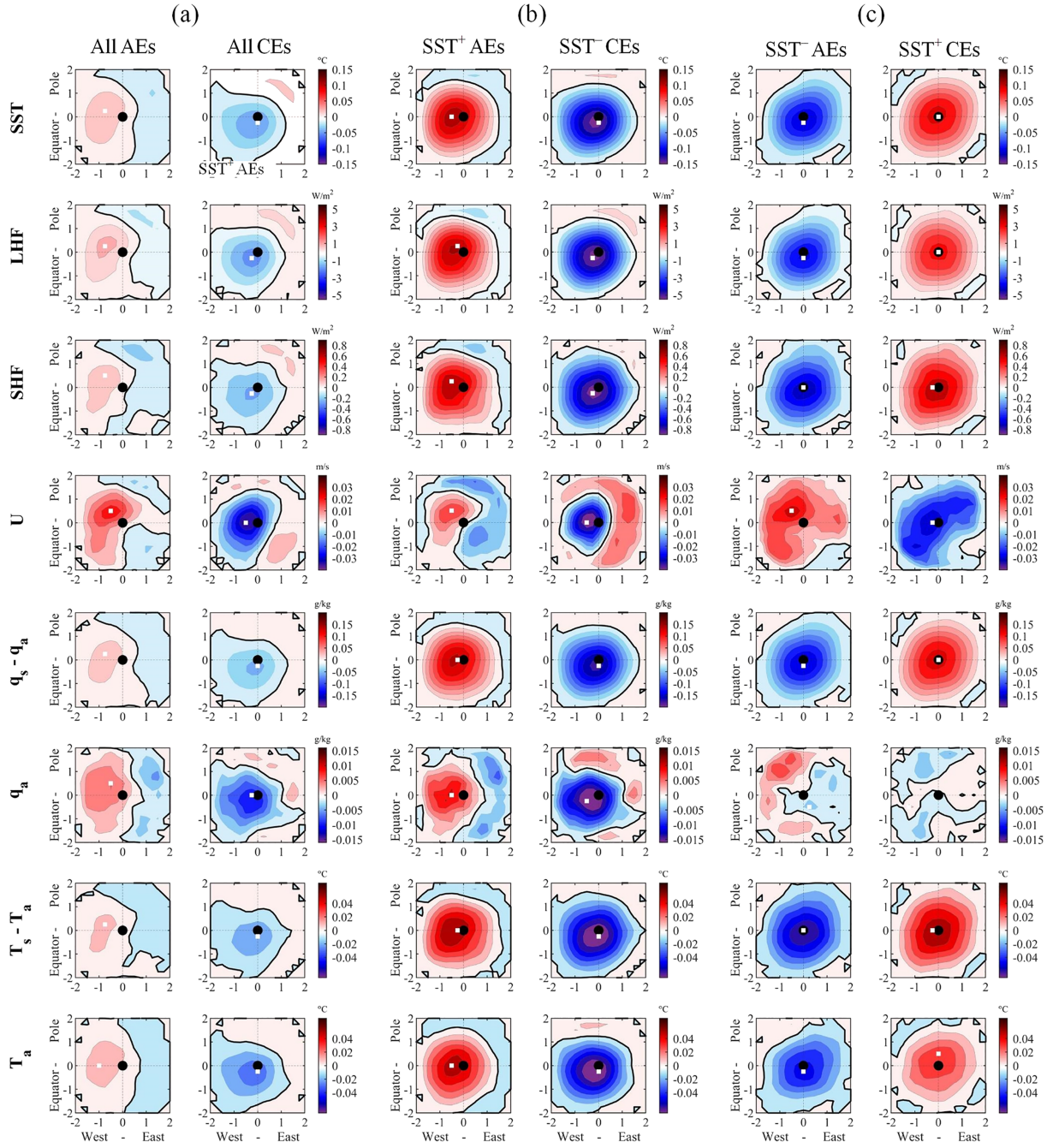

Figure 10. Composite maps of the anomalies in SST, LHF, SHF, U, $q_s - q_a$, q_a, $T_s - T_a$, and T_a over (a) all eddies, (b) SST^+ AEs and SST^- CEs, and (c) SST^- AEs and SST^+ CEs. On each map, a black dot denotes the eddy center, and a white dot denotes the center location of variable (defined by the location of extremum value). Contour intervals are every 0.015 °C for SST, every 0.5 W/m^2 for LHF, every 0.1 W/m^2 for SHF, every 0.005 m/s for U, every 0.02 g/kg for $q_s - q_a$, every 0.002 g/kg for q_a, every 0.01 °C for $T_s - T_a$ and T_a.

Except for the near-linear relationship between SSTA and q_a, U over AEs, positive linear correlations between SSTA and other flux-related variables over eddies are significant. As shown in Figures 12d and 12g, q_a and U increase as SSTA increases before 0.8 °C and then decreases slightly. Similar result has been reported for ocean front and mesoscale eddies in other ocean regions. For instance, Zhang and McPhaden (1995) found that U increases as SSTA smaller than 300 K but decreases when SSTA larger than 300 K for ocean front in the equatorial Pacific. Rouault et al. (2016) also discovered the nonlinear increase of U over warm Agulhas Current eddies.

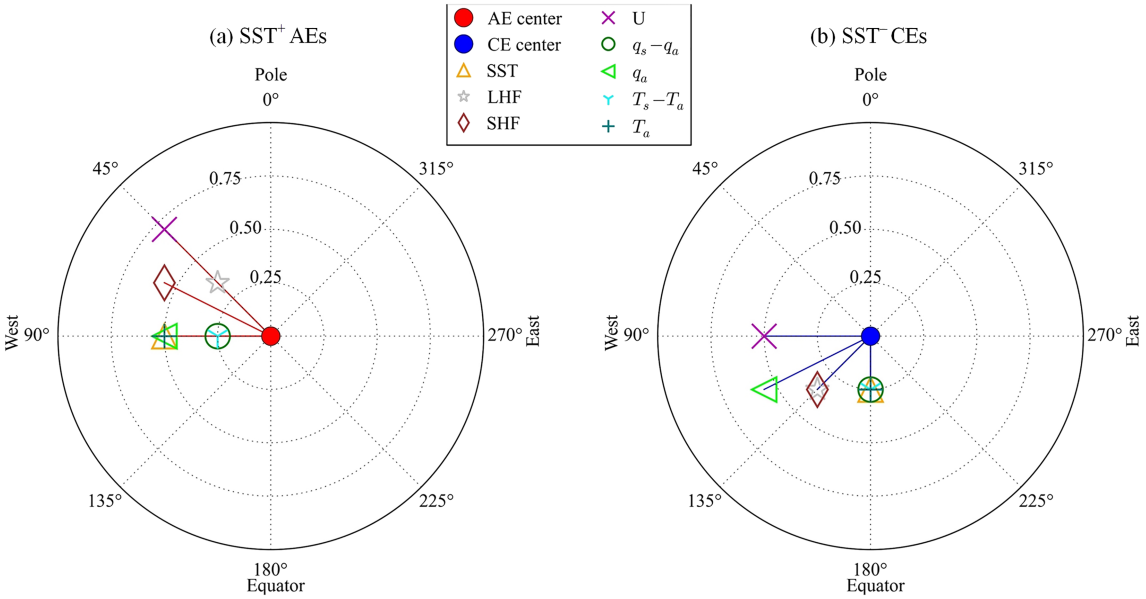

Figure 11. Center locations of SST, LHF, SHF, U, $q_s - q_a$, q_a, $T_s - T_a$, and T_a anomalies relative to (a) the AE center and (b) the CE center constructed from the composites of SST^+ AEs and SST^- CEs, respectively. Axes denote the normalized eddy radius.

To further examine the air-sea coupling over eddies, the coupling strengths between SSTA and LHF, SHF, and flux-related variables are calculated based on their mean anomalies within one eddy radius (Figure 13). Linear correlations are observed between SSTA and LHF, SHF, $q_s - q_a$, $T_s - T_a$, and T_a over eddies. Besides, correlations between SSTA and q_a, U over eddies are weak, especially over AEs. Both q_a and U increase as SSTA increases before 0.4 °C and then decrease slightly. The coupling coefficients for all variables are summarized in Table 3.

4. Summary

Using Advanced Very High Resolution Radiometer-only SST, AVISO SSHA, and newly developed OAFlux satellite-based flux analysis for the 16-year period from 2000 to 2015, the study examined the impact of mesoscale eddies on SST, LHF, SHF, and flux-related surface meteorological variables in the SCS. There are 28,609 AE realizations and 30,381 CE realizations, which correspond to 1,106 AE trajectories and 1,167 CE trajectories, respectively. Major findings are summarized as follows.

Table 2
Mean and Extremum Values ±1 Confidence Interval (CI), and the Variable Center Locations (θ, D) Relative to the Eddy Center for SST, LHF, SHF, U, $q_s - q_a$, q_a, $T_s - T_a$, and T_a over SST^+ AEs and SST^- CEs

Eddy type	SST^+ AEs				SST^- CEs			
Properties	Mean	Maximum	θ	D	Mean	Minimum	θ	D
SST (°C)	0.08 ± 0.001	0.11 ± 0.002	90°	0.5	−0.09 ± 0.001	−0.14 ± 0.002	180°	0.25
LHF (W/m^2)	2.84 ± 0.08	4.07 ± 0.13	45°	0.35	−3.38 ± 0.08	−5.17 ± 0.12	135°	0.35
SHF (W/m^2)	0.47 ± 0.02	0.67 ± 0.04	63.4°	0.56	−0.58 ± 0.02	−0.85 ± 0.03	135°	0.35
U (m/s)	0.004 ± 0.003	0.02 ± 0.004	45°	0.71	−0.01 ± 0.003	−0.04 ± 0.004	90°	0.5
$q_s - q_a$ (g/kg)	0.10 ± 0.002	0.14 ± 0.003	90°	0.25	−0.11 ± 0.002	−0.17 ± 0.003	180°	0.25
q_a (g/kg)	0.005 ± 0.001	0.01 ± 0.002	90°	0.5	−0.01 ± 0.001	−0.02 ± 0.002	116.6°	0.56
$T_s - T_a$ (°C)	0.04 ± 0.001	0.06 ± 0.002	90°	0.25	−0.05 ± 0.001	−0.07 ± 0.002	180°	0.25
T_a (°C)	0.04 ± 0.001	0.06 ± 0.002	90°	0.5	−0.04 ± 0.001	−0.07 ± 0.002	180°	0.25

Note. The CI was computed at the grid point (x, y) where the maximum (minimum) anomalies associated with eddies existed in the composite maps. $CI = 1.96 \times \sigma(X, Y)/\sqrt{N}$, where σ is the standard deviation of eddy-induced anomalies and N is the number of eddy realizations averaged in the composite maps (for CEs, $N = 17{,}700$; for AEs, $N = 16{,}038$). All values are statistically significant at the 95% confidence level.

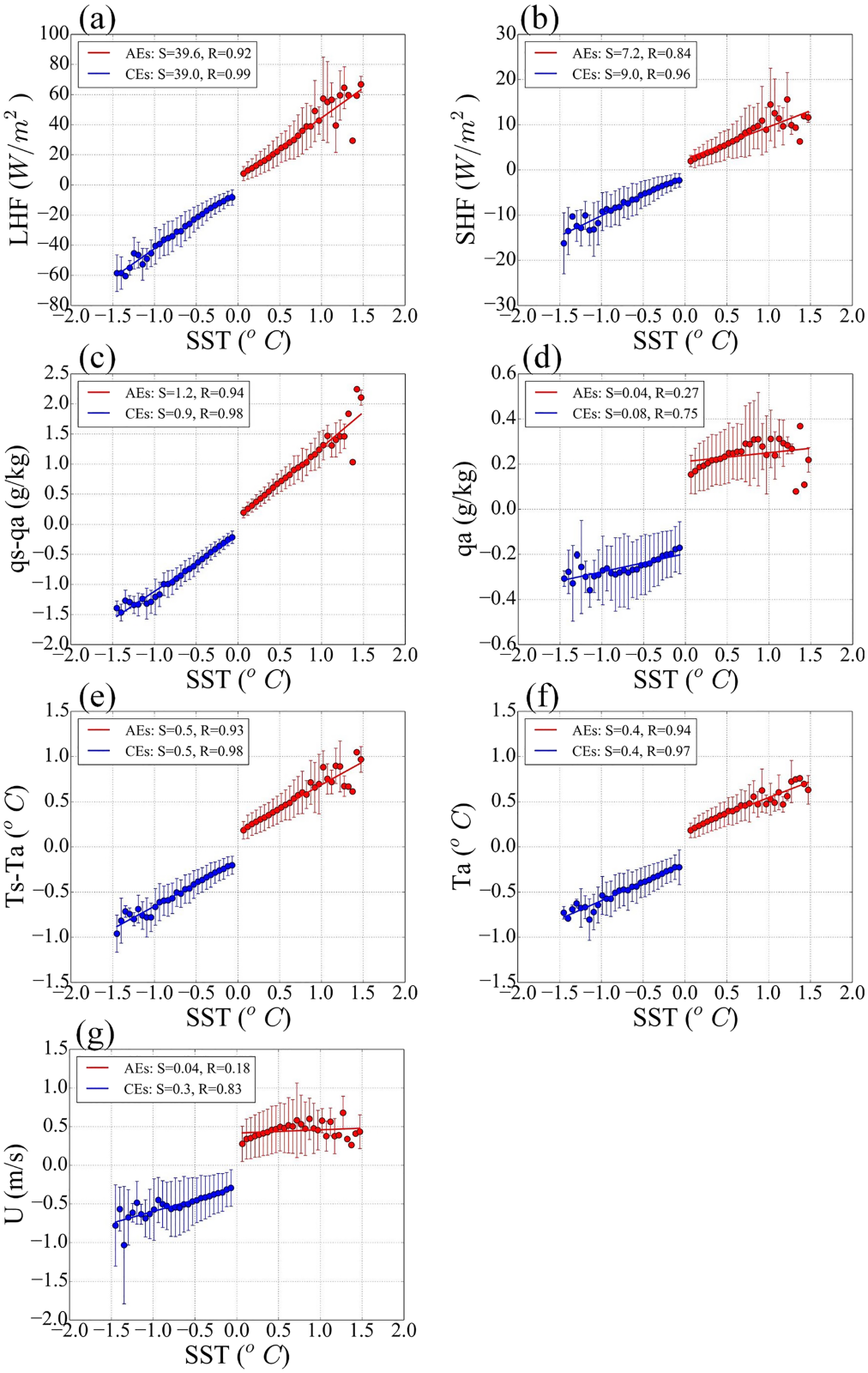

Figure 12. The extreme value within one eddy radius in the anomalies of (a) LHF, (b) SHF, (c) $q_s - q_a$, (d) q_a, (e) $T_s - T_a$, (f) T_a, and (g) U as a function of SSTA. Red colors denote anomalies associated with SST^+ AEs, and blue colors denote those with SST^- CEs. Dots denote the values averaged at the binned SSTA intervals of 0.05 °C, and solid lines denote the regression lines obtained from least squares fitting with S being the slope and R the correlation coefficient.

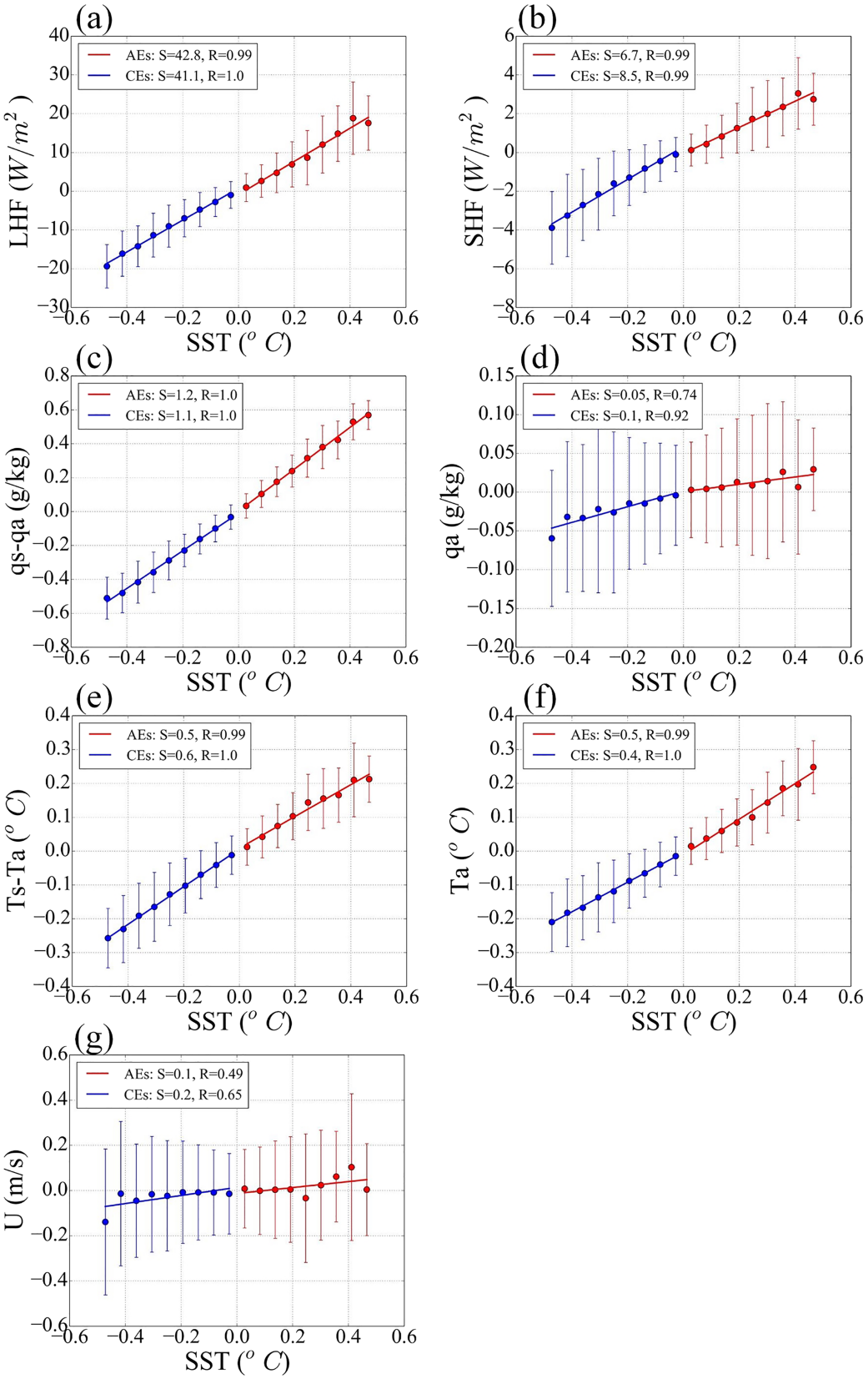

Figure 13. Same as Figure 12 but for the mean anomalies averaged over one eddy radius.

Table 3
Coupling Coefficients of Heat Flux and Flux-Related Variables ±1 CI Over SST^+ AEs and SST^- CEs Obtained From the Least Squares Fitting

Eddy type	SST^+ AEs		SST^- CEs	
Properties	Mean	Maximum	Mean	Minimum
LHF W/m^2 per °C SST	42.8 ± 5.1	39.6 ± 6.5	41.1 ± 2.1	39.0 ± 2.0
SHF W/m^2 per °C SST	6.7 ± 0.9	7.2 ± 1.7	8.5 ± 0.6	9.0 ± 0.96
U m/s per °C SST	0.1 ± 0.09	0.04 ± 0.04	0.2 ± 0.16	0.3 ± 0.08
$q_s - q_a$ g/kg per °C SST	1.2 ± 0.05	1.2 ± 0.15	1.1 ± 0.05	0.9 ± 0.06
q_a g/kg per °C SST	0.05 ± 0.03	0.04 ± 0.04	0.1 ± 0.03	0.08 ± 0.03
$T_s - T_a$ °C per °C SST	0.5 ± 0.05	0.5 ± 0.08	0.6 ± 0.02	0.5 ± 0.04
T_a °C per °C SST	0.5 ± 0.05	0.4 ± 0.04	0.4 ± 0.02	0.4 ± 0.04

Note. All values are significant at the 95% confidence level.

One major finding of the study is that the SST and SSH over eddies are not always positively correlated. This is not consistent with the conventional expectation. In the SCS, the AEs are often not associated with positive SST anomalies, and the CEs are often not associated with negative SST anomalies. We found that only 56% AEs (i.e., 16,038 AEs) are corresponded with positive SSTA and 58% CEs (i.e., 17,700 CEs) are with negative SSTA. Moreover, SST^- AEs and SST^+ CEs occurred at all ranges of eddy amplitude and the whole SCS. The percentage of SST^+ AEs and SST^- CEs relative to the respective total eddies increases slightly with eddy amplitude. Meanwhile, it shows a slight seasonal variation that higher during the winter monsoon months (October–March) and lower during the summer monsoon months (April–September).

Composites of SSTA, LHF, SHF, and flux-related variables are constructed over all eddies, SST^+ eddies, and SST^- eddies, respectively. Spatial patterns of all these composites are asymmetric, of which the extrema shift westward and poleward (equatorward) with respect to eddy center of AEs (CEs). Composites of LHF, SHF $q_s - q_a$, $T_s - T_a$, and T_a show monopole patterns, while composites of U and q_a show dipole patterns. Moreover, the locations of the extrema relative to the eddy centers are slightly different, even over the same type of eddies. As expected, the signs of composites SSTA, LHF, and SHF are positive over SST^+ eddies and negative over SST^- eddies, whereas the sign of composite U is positive over SST^- AEs and negative over SST^+ CEs.

Air-sea coupling associated with SST^+ AEs and SST^- CEs is also examined. There is a strong linear positive correlation between heat flux and SSTA associated with eddies. The coupling strength between SSTA and LHF (SHF) is 39.6 ± 6.5 W/m^2 (7.2 ± 1.7 W/m^2) per degree increase of SST over AEs and 39.0 ± 2.0 W/m^2 (9.0 ± 0.96 W/m^2) per degree decrease of SST over CEs. The couplings between SSTA and other flux-related variables over eddies are positive linear correlated, whereas it is worth noting that the couplings between SSTA and U and q_a over AEs are near linear. As SSTA increases, U and q_a over AEs increase near linearly up to 0.8 °C and then decreases slightly.

In summary, the study provided a statistical characterization of the coupling between SSTA and air-sea heat fluxes and variables over mesoscale eddies in the SCS. However, a few key issues remain to be examined in future work. These include the mechanism controlling the correlation between SST and SSH over mesoscale eddies, the Eulerian eddy tracking approach that was applied in the study, and the cause of a dipole pattern in q_a and U over AEs.

Acknowledgments
This research was conducted while Y. Liu was a visiting graduate student at Woods Hole Oceanographic Institution (WHOI). She sincerely thanks the WHOI Academic Programs Office for hosting her visit and is grateful to the support from China Scholarship Council (CSC). This study was supported by the Strategic Priority Research Program of the Chinese Academy of Sciences (Grant XDA19060101), the Key R & D project of Shandong Province (Grant 2019JZZY010102), the Key deployment project of Center for Ocean Mega-Science, CAS (Grant COMS2019R02), the CAS Program (Grant Y9KY04101L), and the National Natural Science Foundation of China (Grant 41776183 and 41906157). Dr. Xiangze Jin is acknowledged for providing the OAFluxHR analysis and for his programming support and guidance to this study. Heat flux data used in this paper can be downloaded (from https://figshare.com/articles/Eddy-induced_heat_flux_in_the_South_China_Sea/11949735). AVISO SSH data are downloaded from the website (http://www.aviso.altimetry.fr), OISST from the ftp://eclipse.ncdc.noaa.gov/ site, and OAFluxHR analysis will be available from the project website (http://oaflux.whoi.edu).

References

Bôas, A. B. V., Sato, O. T., Chaigneau, A., & Castelão, G. P. (2015). The signature of mesoscale eddies on the air-sea turbulent heat fluxes in the South Atlantic Ocean. *Geophysical Research Letters*, *42*, 1856–1862. https://doi.org/10.1002/2015GL063105

Chaigneau, A., Gizolme, A., & Grados, C. (2008). Mesoscale eddies off Peru in altimeter records: Identification algorithms and eddy spatio-temporal patterns. *Progress in Oceanography*, *79*(2–4), 106–119. https://doi.org/10.1016/j.pocean.2008.10.013

Chaigneau, A., Le Texier, M., Eldin, G., Grados, C., & Pizarro, O. (2011). Vertical structure of mesoscale eddies in the eastern South Pacific Ocean: A composite analysis from altimetry and Argo profiling floats. *Journal of Geophysical Research*, *116*, C12033. https://doi.org/10.1029/2011JC007134

Chelton, D. B., Schlax, M. G., Freilich, M. H., & Milliff, R. F. (2004). Satellite measurements reveal persistent small-scale features in ocean winds. *Science*, *303*(5660), 978–983. https://doi.org/10.1126/science.1091901

Chelton, D. B., Schlax, M. G., & Samelson, R. M. (2011). Global observations of nonlinear mesoscale eddies. *Progress in Oceanography*, *91*(2), 167–216. https://doi.org/10.1016/j.pocean.2011.01.002

Chelton, D. B., & Xie, S. (2010). Coupled ocean-atmosphere interaction at oceanic Mesoscales. *Oceanography*, *23*(4), 52–69. https://doi.org/10.5670/oceanog.2010.05

Chen, G., Gan, J., Xie, Q., Chu, X., Wang, D., & Hou, Y. (2012). Eddy heat and salt transports in the South China Sea and their seasonal modulations. *Journal of Geophysical Research*, *117*, C05021. https://doi.org/10.1029/2011JC007724

Chen, G., Hou, Y., & Chu, X. (2011). Mesoscale eddies in the South China Sea: Mean properties, spatiotemporal variability, and impact on thermohaline structure. *Journal of Geophysical Research*, *116*, C06018. https://doi.org/10.1029/2010JC006716

Chen, L., Jia, Y., & Liu, Q. (2017). Oceanic eddy-driven atmospheric secondary circulation in the winter Kuroshio Extension region. *Journal of Oceanography*, *73*(3), 295–307. https://doi.org/10.1007/s10872-016-0403-z

Cheng, X., & Qi, Y. (2010). Variations of eddy kinetic energy in the South China Sea. *Journal of Oceanography*, *66*(1), 85–94. https://doi.org/10.1007/s10872-010-0007-y

Cheng, Y.-H., Ho, C.-R., Zheng, Q., & Kuo, N.-J. (2014). Statistical characteristics of mesoscale eddies in the North Pacific derived from satellite altimetry. *Remote Sensing*, *6*(6), 5164–5183. https://doi.org/10.3390/rs6065164

Chow, C.-H., Hu, J.-H., Centurioni, L. R., & Niiler, P. P. (2008). Mesoscale Dongsha cyclonic eddy in the northern South China Sea by drifter and satellite observations. *Journal of Geophysical Research*, *113*, C04018. https://doi.org/10.1029/2007jc004542

Chow, C. H., & Liu, Q. (2012). Eddy effects on sea surface temperature and sea surface wind in the continental slope region of the northern South China Sea. *Geophysical Research Letters*, *39*, L02601. https://doi.org/10.1029/2011GL050230

Doglioli, A. M., Blanke, B., Speich, S., & Lapeyre, G. (2007). Tracking coherent structures in a regional ocean model with wavelet analysis: Application to Cape Basin eddies. *Journal of Geophysical Research*, *112*, C05043. https://doi.org/10.1029/2006jc003952

Du, Y., Wu, D., Liang, F., Yi, J., Mo, Y., He, Z., & Pei, T. (2016). Major migration corridors of mesoscale ocean eddies in the South China Sea from 1992 to 2012. *Journal of Marine Systems*, *158*, 173–181. https://doi.org/10.1016/j.jmarsys.2016.01.013

Ducet, N., Le Traon, P. Y., & Reverdin, G. (2000). Global high-resolution mapping of ocean circulation from TOPEX/Poseidon and ERS-1 and -2. *Journal of Geophysical Research*, *105*(C8), 19,477–19,498. https://doi.org/10.1029/2000JC900063

Everett, J. D., Baird, M. E., Oke, P. R., & Suthers, I. M. (2012). An avenue of eddies: Quantifying the biophysical properties of mesoscale eddies in the Tasman Sea. *Geophysical Research Letters*, *39*, L16608. https://doi.org/10.1029/2012GL053091

Faghmous, J. H., Frenger, I., Yao, Y., Warmka, R., Lindell, A., & Kumar, V. (2015). A daily global mesoscale ocean eddy dataset from satellite altimetry. *Scientific data*, *2*, 150,028. https://doi.org/10.1038/sdata.2015.28

Fairall, C., Bradley, E. F., Hare, J., Grachev, A., & Edson, J. (2003). Bulk parameterization of air–sea fluxes: Updates and verification for the COARE algorithm. *Journal of Climate*, *16*(4), 571–591. https://doi.org/10.1175/1520-0442(2003)016<0571:BPOASF>2.0.CO;2

Frenger, I., Gruber, N., Knutti, R., & Münnich, M. (2013). Imprint of Southern Ocean eddies on winds, clouds and rainfall. *Nature Geoscience*, *6*(8), 608–612. https://doi.org/10.1038/ngeo1863

Gaube, P., Chelton, D. B., Samelson, R. M., Schlax, M. G., & O'Neill, L. W. (2015). Satellite observations of mesoscale eddy-induced Ekman pumping. *Journal of Physical Oceanography*, *45*(1), 104–132. https://doi.org/10.1175/jpo-d-14-0032.1

Guo, M., Chai, F., Peng, X., Li, S., & Rao, S. (2015). Impacts of mesoscale eddies in the South China Sea on biogeochemical cycles. *Ocean Dynamics*, *65*(9–10), 1335–1352.

Hausmann, U., & Czaja, A. (2012). The observed signature of mesoscale eddies in sea surface temperature and the associated heat transport. *Deep Sea Research Part I: Oceanographic Research Papers*, *70*, 60–72. https://doi.org/10.1016/j.dsr.2012.08.005

Hayes, S., McPhaden, M., & Wallace, J. (1989). The influence of sea-surface temperature on surface wind in the eastern equatorial Pacific: Weekly to monthly variability. *Journal of Climate*, *2*(12), 1500–1506. https://doi.org/10.1175/1520-0442(1989)002<1500:tiosst>2.0.co;2

He, Q., Zhan, H., Cai, S., He, Y., Huang, G., & Zhan, W. (2018). A new assessment of mesoscale eddies in the South China Sea: Surface features, three-dimensional structures, and thermohaline transports. *Journal of Geophysical Research: Oceans*, *123*, 4906–4929. https://doi.org/10.1029/2018JC014054

Hilburn, K., & Wentz, F. (2008). Mitigating the impact of RADCAL beacon contamination on F15 SSM/I ocean retrievals. *Geophysical Research Letters*, *35*, L18806. https://doi.org/10.1029/2008GL034914

Hwang, C., & Chen, S.-A. (2000). Circulations and eddies over the South China Sea derived from TOPEX/Poseidon altimetry. *Journal of Geophysical Research*, *105*(C10), 23,943–23,965. https://doi.org/10.1029/2000jc900092

Isern-Fontanet, J., García-Ladona, E., & Font, J. (2003). Identification of marine eddies from altimetric maps. *Journal of Atmospheric and Oceanic Technology*, *20*(5), 772–778. https://doi.org/10.1175/1520-0426(2003)20<772:IOMEFA>2.0.CO;2

Jia, Y., & Liu, Q. (2004). Eddy shedding from the Kuroshio Bend at Luzon Strait. *Journal of Oceanography*, *60*(6), 1063–1069. https://doi.org/10.1007/s10872-005-0014-6

Kurian, J., Colas, F., Capet, X., McWilliams, J. C., & Chelton, D. B. (2011). Eddy properties in the California Current System. *Journal of Geophysical Research*, *116*, C08027. https://doi.org/10.1029/2010JC006895

Le Traon, P. Y., & Dibarboure, G. (1999). Mesoscale mapping capabilities of multiple-satellite altimeter missions. *Journal of Atmospheric and Oceanic Technology*, *16*(9), 1208–1223. https://doi.org/10.1175/1520-0426(1999)016<1208:MMCOMS>2.0.CO;2

Leyba, I. M., Saraceno, M., & Solman, S. A. (2017). Air-sea heat fluxes associated to mesoscale eddies in the Southwestern Atlantic Ocean and their dependence on different regional conditions. *Climate Dynamics*, *49*(7–8), 2491–2501. https://doi.org/10.1007/s00382-016-3460-5

Liu, H., Li, W., Chen, S., Fang, R., & Li, Z. (2018). Atmospheric response to mesoscale ocean eddies over the South China Sea. *Advances in Atmospheric Sciences*, *35*(9), 1189–1204. https://doi.org/10.1007/s00376-018-7175-x

Liu, Q., Jia, Y., Liu, P., Wang, Q., & Chu, P. C. (2001). Seasonal and intraseasonal thermocline variability in the central South China Sea. *Geophysical Research Letters*, *28*(23), 4467–4470. https://doi.org/10.1029/2001gl013185

Liu, Q., Kaneko, A., & Jilan, S. (2008). Recent progress in studies of the South China Sea circulation. *Journal of Oceanography*, *64*(5), 753–762. https://doi.org/10.1007/s10872-008-0063-8

Liu, Y., Chen, G., Sun, M., Liu, S., & Tian, F. (2016). A parallel SLA-based algorithm for global mesoscale eddy identification. *Journal of Atmospheric and Oceanic Technology*, *33*(12), 2743–2754. https://doi.org/10.1175/JTECH-D-16-0033.1

Ma, X., Jing, Z., Chang, P., Liu, X., Montuoro, R., Small, R. J., et al. (2016). Western boundary currents regulated by interaction between ocean eddies and the atmosphere. *Nature*, *535*(7613), 533–537. https://doi.org/10.1038/nature18640

Morrow, R., Carret, A., Birol, F., Nino, F., Valladeau, G., Boy, F., et al. (2017). Observability of fine-scale ocean dynamics in the northwestern Mediterranean Sea. *Ocean Science*, *13*(1), 13–29. https://doi.org/10.5194/os-13-13-2017

Nencioli, F., Dong, C., Dickey, T., Washburn, L., & McWilliams, J. C. (2010). A vector geometry–based eddy detection algorithm and its application to a high-resolution numerical model product and high-frequency radar surface velocities in the Southern California Bight. *Journal of Atmospheric and Oceanic Technology*, *27*(3), 564–579. https://doi.org/10.1175/2009jtecho725.1

O'Neill, L. W., Esbensen, S. K., Thum, N., Samelson, R. M., & Chelton, D. D. (2010). Dynamical analysis of the boundary layer and surface wind responses to mesoscale SST perturbations. *Journal of Climate*, *23*(3), 559. https://doi.org/10.1175/2009JCLI2662.1

Pascual, A., Pujol, M.-I., Larnicol, G., Le Traon, P.-Y., & Rio, M.-H. (2007). Mesoscale mapping capabilities of multisatellite altimeter missions: First results with real data in the Mediterranean Sea. *Journal of Marine Systems*, *65*(1–4), 190–211. https://doi.org/10.1016/j.jmarsys.2004.12.004

Pujol, M.-I., Faugère, Y., Taburet, G., Dupuy, S., Pelloquin, C., Ablain, M., & Picot, N. (2016). DUACS DT2014: The new multi-mission altimeter data set reprocessed over 20 years. *Ocean Science*, *12*(5), 1067–1090. https://doi.org/10.5194/os-12-1067-2016

Putrasahan, D. A., Kamenkovich, I., Le Hénaff, M., & Kirtman, B. P. (2017). Importance of ocean mesoscale variability for air-sea interactions in the Gulf of Mexico. *Geophysical Research Letters*, *44*, 6352–6362. https://doi.org/10.1002/2017GL072884

Reynolds, R. W., Smith, T. M., Liu, C., Chelton, D. B., Casey, K. S., & Schlax, M. G. (2007). Daily high-resolution-blended analyses for sea surface temperature. *Journal of Climate*, *20*(22), 5473–5496. https://doi.org/10.1175/2007JCLI1824.1

Rouault, M., Verley, P., & Backeberg, B. (2016). Wind changes above warm Agulhas Current eddies. *Ocean Science*, *12*(2), 495–506. https://doi.org/10.5194/os-12-495-2016

Small, R. J., deSzoeke, S. P., Xie, S. P., O'Neill, L., Seo, H., Song, Q., et al. (2008). Air–sea interaction over ocean fronts and eddies. *Dynamics of Atmospheres and Oceans*, *45*(3–4), 274–319. https://doi.org/10.1016/j.dynatmoce.2008.01.001

Song, Q., Cornillon, P., & Hara, T. (2006). Surface wind response to oceanic fronts. *Journal of Geophysical Research*, *111*, C12006. https://doi.org/10.1029/2006jc003680

Sun, S., Fang, Y., Liu, B., & Tana (2016). Coupling between SST and wind speed over mesoscale eddies in the South China Sea. *Ocean Dynamics*, *66*(11), 1467–1474. https://doi.org/10.1007/s10236-016-0993-4

Sun, W., Dong, C., Tan, W., & He, Y. (2019). Statistical characteristics of cyclonic warm-core eddies and anticyclonic cold-core eddies in the North Pacific based on remote sensing data. *Remote Sensing*, *11*(2), 208. https://doi.org/10.3390/rs11020208

Wallace, J. M., Mitchell, T. P., & Deser, C. (1989). The influence of sea-surface temperature on surface wind in the eastern equatorial Pacific: Seasonal and interannual variability. *Journal of Climate*, *2*(12), 1492–1499. https://doi.org/10.1175/1520-0442(1989)002<1492:TIOSST>2.0.CO;2

Wang, D., Xu, H., Lin, J., & Hu, J. (2008). Anticyclonic eddies in the northeastern South China Sea during winter 2003/2004. *Journal of Oceanography*, *64*(6), 925–935. https://doi.org/10.1007/s10872-008-0076-3

Wang, G. (2003). Mesoscale eddies in the South China Sea observed with altimeter data. *Geophysical Research Letters*, *30*(21), 2247. https://doi.org/10.1029/2003gl018532

Wang, G., Chen, D., & Su, J. (2008). Winter eddy genesis in the eastern South China Sea due to orographic wind jets. *Journal of Physical Oceanography*, *38*(3), 726–732. https://doi.org/10.1175/2007jpo3868.1

Wang, Y., Olascoaga, M. J., & Beron-Vera, F. J. (2015). Coherent water transport across the South Atlantic. *Geophysical Research Letters*, *42*, 4072–4079. https://doi.org/10.1002/2015gl064089

Xie, S.-P. (2004). Satellite observations of cool ocean–atmosphere interaction. *Bulletin of the American Meteorological Society*, *85*(2), 195–208. https://doi.org/10.1175/BAMS-85-2-195

Xiu, P., & Chai, F. (2011). Modeled biogeochemical responses to mesoscale eddies in the South China Sea. *Journal of Geophysical Research*, *116*, C10006. https://doi.org/10.1029/2010JC006800

Xiu, P., Chai, F., Shi, L., Xue, H., & Chao, Y. (2010). A census of eddy activities in the South China Sea during 1993–2007. *Journal of Geophysical Research*, *115*, C03012. https://doi.org/10.1029/2009jc005657

Yu, L. (2019). Global air–sea fluxes of heat, fresh water, and momentum: Energy budget closure and unanswered questions. *Annual Review of Marine Science*, *11*, 227–248. https://doi.org/10.1146/annurev-marine-010816-060704

Yu, L., & Jin, X. (2014). Confidence and sensitivity study of the OAFlux multisensor synthesis of the global ocean surface vector wind from 1987 onward. *Journal of Geophysical Research: Oceans*, *119*, 6842–6862. https://doi.org/10.1002/2014JC010194

Yu, L., & Jin, X. (2018). A regime-dependent retrieval algorithm for near-surface air temperature and specific humidity from multi-microwave sensors. *Remote Sensing of Environment*, *215*, 199–216. https://doi.org/10.1016/j.rse.2018.06.001

Yu, L., Jin, X., & Weller, R. A. (2008). Multidecade global flux datasets from the objectively analyzed air-sea fluxes (OAFlux) project: Latent and sensible heat fluxes, ocean evaporation, and related surface meteorological variables. OAFlux project technical report. OA-2008-01. Retrieved from http://oaflux.whoi.edu/pdfs/OAFlux_TechReport_3rd_release.pdf

Yu, L., & Weller, R. A. (2007). Objectively analyzed air–sea heat fluxes for the global ice-free oceans (1981–2005). *Bulletin of the American Meteorological Society*, *88*(4), 527–540. https://doi.org/10.1175/BAMS-88-4-527

Zhang, G., & McPhaden, M. J. (1995). The relationship between sea surface temperature and latent heat flux in the equatorial Pacific. *Journal of Climate*, *8*, 589–605. https://doi.org/10.1175/1520-0442(1995)0082.0.CO;2

Zhang, Z., Tian, J., Qiu, B., Zhao, W., Chang, P., Wu, D., & Wan, X. (2016). Observed 3D structure, generation, and dissipation of oceanic mesoscale eddies in the South China Sea. *Scientific Reports*, *6*, 24,349. https://doi.org/10.1038/srep24349

Zhuang, W., Du, Y., Wang, D., Xie, Q., & Xie, S. (2010). Pathways of mesoscale variability in the South China Sea. *Chinese Journal of Oceanology and Limnology*, *28*(5), 1055–1067. https://doi.org/10.1007/s00343-010-0035-x

Zhuang, W., Xie, S.-P., Wang, D., Taguchi, B., Aiki, H., & Sasaki, H. (2010). Intraseasonal variability in sea surface height over the South China Sea. *Journal of Geophysical Research*, *115*, C04010. https://doi.org/10.1029/2009jc005647